CSMA 2026
17ème Colloque National en Calcul des Structures
18-22 Mai 2026, Presqu'île de Giens (Var)

Truss topology optimization for ultralight aeronautical structures

E. Stragiotti[1,2], C. Julien[1], FX. Irisarri[1], J. Morlier[3]

[1] *DMAS, ONERA, Université Paris-Saclay, Châtillon, F-92322, France*
[2] *Institut Clément Ader, Université de Toulouse, ISAE-SUPAERO-CNRS-INSA-Mines Albi-UPS, 3, Rue Caroline Aigle, Toulouse, 31400, France*
[3] *ISAE-SUPAERO, Université de Toulouse, France*

Résumé — Ultralight trusses are ideal for innovative aero-structures due to their high stiffness-to-weight ratio and favorable aeroelastic properties. Their design must account for mechanical constraints, including maximum stress and local buckling. This work formulates a volume minimization problem for 3D structures under multiple load cases, stress, and topological buckling constraints. A two-step optimization strategy is used : first, a relaxed problem is solved via Sequential Linear Programming to explore the design space ; second, the full nonlinear problem is refined using IPOPT to satisfy all mechanical constraints. The method is applied to the 3D wingbox of the Common Research Model, considering different materials—aluminum, titanium, stainless steel, and pultruded CFRP—and the environmental impact in terms of CO_2^{eq} is evaluated.
Mots clés — Lattice structures, Topology Optimization, Non Linear Programming, Buckiling contraints

1 Introduction

Ultralight trusses are well-suited for innovative aerostructures due to their high stiffness-to-weight ratio and favorable aeroelastic properties [1]. Previous works [2, 3] used two-step sequential optimization to reduce truss weight : generating a stress-informed ground structure and sizing cross-sectional areas considering stress, local buckling, and aeroelastic constraints. Alternatively, [4] employed discrete cross-sectional areas with a Mixed Integer Linear Optimization (MILO) algorithm on a 315-bar CRM wingbox. While sizing optimization simplifies numerical challenges, it limits the potential for topological improvements. This paper formulates a volume minimization problem for 3D trusses under multiple load cases, stress, and local buckling constraints, iteratively modifying topology to find innovative configurations. Due to non-linear buckling and kinematic compatibility constraints, the problem is non-convex and initialization-dependent. A two-step optimization with a heuristic strategy is proposed to address numerical difficulties and reduce sensitivity to the starting point. The paper introduces topological buckling and kinematic constraints (Sec. 2), details the two-step optimization and heuristic method (Sec. 3), and applies the approach to a full-scale CRM wingbox with different materials and environmental impact analysis (Sec. 4).

2 Background

2.1 Truss topology optimization (TTO)

The optimization problem is formulated within the TTO framework. It involves selecting the cross-sectional areas $\boldsymbol{a}$ and the connectivity of a discrete and dense bar mesh called the ground structure [5]. Since the nodes within the ground structure are considered as pin-joints, all straight members exclusively experience either tension or compression loads. The optimization formulation that is used as the foundation of the proposed method is stated in terms of members' cross-sectional areas $\boldsymbol{a}$ and member forces $\boldsymbol{q}$ as follows :

$$\mathbb{P}_0 : \begin{aligned} \min_{\boldsymbol{a},\boldsymbol{q}} \quad & V = \boldsymbol{l}^\top \boldsymbol{a}, \qquad \boldsymbol{a} \geq 0, \quad \text{(Volume)} \\ \text{s.t.} \quad & \boldsymbol{B}\boldsymbol{q} = \boldsymbol{f} \quad \text{(Force equilibrium)} \\ & -\boldsymbol{\sigma}_c \boldsymbol{a} \leq \boldsymbol{q} \leq \boldsymbol{\sigma}_t \boldsymbol{a} \quad \text{(Stress constraints)} \end{aligned} \tag{1}$$

where $\boldsymbol{B}$ is an $N_{\text{dof}} \times N_{\text{el}}$ matrix containing the direction cosines of the j-th member with respect to the i-th degree of freedom to calculate the nodal force equilibrium, and where N_{dof} is the number of Degrees of Freedom (DOFs), equal to $2M$ or $3M$ for a two- or three-dimensional load case, respectively. vector $\boldsymbol{q} = [q_1, q_2, \ldots, q_{N_{\text{el}}}]^T$ is the vector containing the internal member forces, with a positive sign when in tension, caused by the external load $\boldsymbol{f} = [f_1, f_2, \ldots, f_{N_{\text{dof}}}]^T$. The state variable $\boldsymbol{a} = [a_1, a_2, \ldots, a_{N_{\text{el}}}]^T$ represents the cross-sectional areas of the N_{el} members of the structure and $\boldsymbol{l} = [l_1, l_2, \ldots, l_{N_{\text{el}}}]^T$ is the vector of element length. Parameters σ_c and σ_t are the compressive and tensile maximum allowable stresses of the material, respectively.

2.2 Local and topological buckling constraints

Local buckling constraints are critical in ultralight truss optimization, as such structures are often governed by Euler buckling. With zero lower bounds on member areas, the feasible region becomes disjoint [6], and optimal solutions lie in a singular subset of the design space [7]. Using a SAND formulation with local buckling and kinematic compatibility allows to size in the optimization loop, though the NLP remains sensitive to initialization [8]. Local buckling constraints are expressed as

$$\boldsymbol{g}_{\text{buck}} := q_i + \frac{s a_i^2}{\ell_i^2} \geq 0, \qquad s = \pi^2 E \beta, \tag{2}$$

where β depends on the cross-section shape and E is Young's modulus. Directly imposing (2) can produce compressive chains of unstable members, causing topological buckling [9, 10]. Post-processing such chains reduces optimality. To incorporate topological effects, an adaptive buckling length is defined :

$$l_i^*(\boldsymbol{a}) := \begin{cases} l_i, & i \notin \mathcal{C}_{l,r}(\boldsymbol{a}), \\ \sum_{r \in \mathcal{C}_{l,r}(\boldsymbol{a})} l_r, & i \in \mathcal{C}_{l,1}(\boldsymbol{a}), \end{cases} \tag{3}$$

where $\mathcal{C}_{l,r}(\boldsymbol{a})$ is the set of members in the l-th compressive chain. Side constraints ensure non-decreasing cross-sectional areas along each chain :

$$a_r \geq a_{r=1}, \qquad r \in \mathcal{C}_{l,r}(\boldsymbol{a}),\ r \neq 1. \tag{4}$$

2.3 Kinematic Compatibility Constraints

To optimize test cases that result in statically indeterminate structures, such as structures loaded with multiple load cases or imposed symmetries, we add an additional mechanical constraint called kinematic compatibility [11]. Compatibility can be taken into account by imposing a nonlinear constraint in the optimization formulation [12]. The kinematic compatibility constraints restrict the displacement field $\boldsymbol{U} = [U_1, \ldots, U_{N_{\text{dof}}}]^T$ in such a way that strains ε_i and internal stresses σ_i comply with Hooke's law $\sigma_i = E_i \varepsilon_i$ with $i \in [1, \ldots, N_{\text{el}}]$. Recalling that in a truss the relationship between nodal displacements and member deformations is $\boldsymbol{b}_i^\top \boldsymbol{U} = \ell_i \varepsilon_i$ with $\boldsymbol{b}_i$ as the i-th column of the $\boldsymbol{B}$ matrix, we can formulate the kinematic compatibility constraints $\boldsymbol{g}_{\text{comp}}$ as :

$$\boldsymbol{g}_{\text{comp}} := q_i - \frac{a_i E_i}{\ell_i} \boldsymbol{b}_i^\top \boldsymbol{U} = 0. \quad \forall i \in [1, \ldots, N_{\text{el}}] \tag{5}$$

Kinematic compatibility constraints are non-linear as the design variable $\boldsymbol{q}$ is dependent on $\boldsymbol{a}$ and $\boldsymbol{U}$.

3 Optimization formulation and solving strategy

We propose a TTO formulation for minimizing the mass of 3D ultralight truss structures under maximum stress, topological buckling, and kinematic compatibility constraints. Combining Formulation $(\mathbb{P}_0)$ with Equations (2), (3), and (4), the complete formulation $(\mathbb{P}_1)$ is expressed in terms of cross-sectional

areas $\boldsymbol{a}$, member forces $\boldsymbol{q}$, and nodal displacements $\boldsymbol{U}$:

$$
\begin{aligned}
\min_{\boldsymbol{a},\boldsymbol{q}^0,\ldots,\boldsymbol{q}^{N_p},\boldsymbol{U}^0,\ldots,\boldsymbol{U}^{N_p}} \quad & V = \boldsymbol{\ell}^T \boldsymbol{a} \\
\text{s.t. } & \boldsymbol{B}\boldsymbol{q}^p = \boldsymbol{f}^p, \quad \boldsymbol{q}^p = \frac{\boldsymbol{a}E}{\boldsymbol{\ell}} \boldsymbol{b}^T \boldsymbol{U}^p, \quad \boldsymbol{q}^p \geq -\frac{s\boldsymbol{a}^2}{\boldsymbol{\ell}^{*2}}, \quad -\sigma_c \boldsymbol{a} \leq \boldsymbol{q}^p \leq \sigma_t \boldsymbol{a}, \quad \forall p, \\
& a_r \geq a_{r=1}, \quad r \in \mathcal{C}_{l,r}(\boldsymbol{a}), \\
& 0 \leq \boldsymbol{a} \leq \frac{4\pi\boldsymbol{\ell}^2}{\lambda_{\max}}.
\end{aligned}
\tag{$\mathbb{P}_1$}
$$

The formulation supports multiple load cases N_p with external loads $\boldsymbol{f}^0, \ldots, \boldsymbol{f}^{N_p}$, producing internal forces $\boldsymbol{q} = [\boldsymbol{q}^0, \ldots, \boldsymbol{q}^{N_p}]$ and displacements $\boldsymbol{U} = [\boldsymbol{U}^0, \ldots, \boldsymbol{U}^{N_p}]$. It extends the multi-load formulation of [10] by including kinematic compatibility, enabling correct evaluation of statically indeterminate structures. The method follows the SAND paradigm [13], treating $\boldsymbol{a}$, $\boldsymbol{q}$, and $\boldsymbol{U}$ as independent design variables. This simplifies sensitivity calculations, preserves sparsity, avoids solving the stiffness equation $\boldsymbol{K}\boldsymbol{U} = \boldsymbol{f}$ during optimization, and eliminates the need for lower bounds on $\boldsymbol{a}$. Since $\boldsymbol{U}$ are explicit variables, displacement bounds can be imposed directly.

3.1 Optimization Strategy

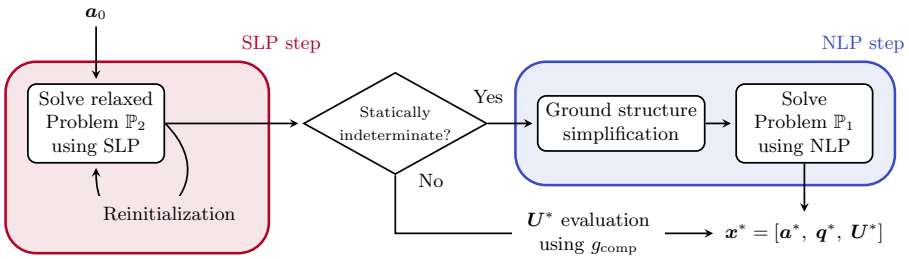

FIGURE 1 – Flowchart of the two-step optimization strategy for Problem $(\mathbb{P}_1)$.

Problem $(\mathbb{P}_1)$ features many constraints and variables per bar, producing a highly non-linear design space where a direct NLP solve typically yields dense, intersecting trusses. To address this, we introduce a two-step strategy [**?**] : a relaxed optimization finds a clean initial design, and a second optimization enforces all mechanical constraints (Fig. 1). In the first step, kinematic compatibility is removed, producing the relaxed Problem $(\mathbb{P}_2)$. This problem is solved with Sequential Linear Programming (SLP), where buckling constraints are iteratively linearized. A reinitialization heuristic mitigates dependence on the starting point $\boldsymbol{a}_0$. The resulting solution $\tilde{\boldsymbol{x}}^*$ is post-processed by removing members with areas below a fixed threshold, producing simpler, sparser structures than direct NLP on $(\mathbb{P}_1)$. If the SLP result is statically determinate, the optimization ends, since (5) then gives the correct displacements. If the structure is statically indeterminate, a second step is required. The ground structure is reduced to include only members active in the SLP solution, preventing reintroduction of discarded bars. Then kinematic compatibility and exact local buckling constraints are reinstated, and Problem $(\mathbb{P}_1)$ is solved on the reduced ground structure using an NLP solver, initialized with $\tilde{\boldsymbol{x}}^*$.

3.2 First step : SLP optimization

In the first stage of the proposed strategy,the relaxed Problem $(\mathbb{P}_2)$ is solved. This problem is obtained from $(\mathbb{P}_1)$ by removing the compatibility constraint (5) and the displacement variables $\boldsymbol{U}$:

$$
\begin{aligned}
\min_{\boldsymbol{a},\boldsymbol{q}^0,\ldots,\boldsymbol{q}^P} \quad & V = \boldsymbol{\ell}^T \boldsymbol{a} \\
\text{s.t. } & \boldsymbol{B}\boldsymbol{q}^p = \boldsymbol{f}^p, \quad \boldsymbol{q}^p \geq -\frac{s\boldsymbol{a}^2}{\boldsymbol{\ell}^{*2}}, \quad -\sigma_c \boldsymbol{a} \leq \boldsymbol{q}^p \leq \sigma_t \boldsymbol{a}, \quad \forall p \in [0, \ldots, N_p], \\
& a_r \geq a_{r=1}, \quad r \in \mathcal{C}_{l,r}(\boldsymbol{a}), \\
& 0 \leq \boldsymbol{a} \leq \frac{4\pi\boldsymbol{\ell}^2}{\lambda_{\max}}.
\end{aligned}
\tag{$\mathbb{P}_2$}
$$

All constraints are linear except the local buckling condition. Therefore, we apply a Sequential Linear Programming (SLP) scheme, linearizing the buckling constraint at each iteration. Following [14], the Euler critical load for member i is expanded via a first-order Taylor approximation around the current iterate a_i^k :

$$\tilde{q}_{i,k}^{\text{cr}} = q_{i,k}^{\text{cr}}(a_i^k) + (a_i^{k+1} - a_i^k) \left. \frac{\partial q_{i,k}^{\text{cr}}}{\partial a} \right|_{a=a_i^k}, \tag{6}$$

where $q_{i,k}^{\text{cr}}(a_i^k) = -s(a_i^k)^2/\ell_i^{*2}$. This yields the linearized buckling constraint

$$q_i \geq \tilde{q}_{i,k}^{\text{cr}} = -\frac{s\, a_i^k (2a_i^{k+1} - a_i^k)}{\ell_i^{*2}} \qquad \forall i \in [1, \ldots, N_{\text{el}}]. \tag{7}$$

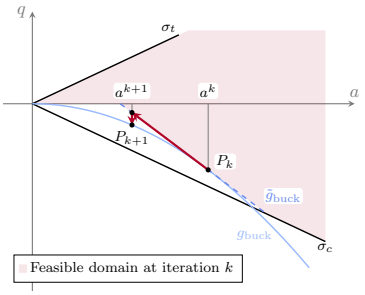

FIGURE 2 – Linearization of the local buckling constraint for bar i at iterate a_i^k.

Substituting (7) into ($\mathbb{P}_2$) gives the linearized subproblem (the design variables are the sections a and also the loads q) :

$$\begin{aligned} \min_{\boldsymbol{a}, \boldsymbol{q}^0, \ldots, \boldsymbol{q}^P} \; & V = \boldsymbol{\ell}^T \boldsymbol{a} \\ \text{s.t. } & \boldsymbol{B}\boldsymbol{q}^p = \boldsymbol{f}^p, \qquad \boldsymbol{q}^p \geq -\frac{s\, \boldsymbol{a}^k (2\boldsymbol{a}^{k+1} - \boldsymbol{a}^k)}{\boldsymbol{\ell}^{*2}}, \qquad -\sigma_c \boldsymbol{a} \leq \boldsymbol{q}^p \leq \sigma_t \boldsymbol{a}, \quad \forall p, \\ & a_r \geq a_{r=1}, \quad r \in \mathcal{C}_{l,r}(\boldsymbol{a}), \\ & 0 \leq \boldsymbol{a} \leq \frac{4\pi\ell^2}{\lambda_{\max}}. \end{aligned} \tag{$\tilde{\mathbb{P}}_2$}$$

Because this subproblem is fully linear, it can be solved using a standard LP solver. At iteration k, the current vector $\boldsymbol{a}^k$ defines the linearization point $\boldsymbol{P}_k$. Solving ($\tilde{\mathbb{P}}_2$) produces the updated areas $\boldsymbol{a}^{k+1}$, which are then used to relinearize the buckling constraint at the next iteration. This process repeats until

$$\|\Delta \boldsymbol{x}\|_\infty \leq \text{tol}_{\text{slp}},$$

where $\Delta \boldsymbol{x}$ is the change in design variables between successive iterations.

3.3 Handling local minima : reinitialization strategy

When the cross-sectional area of bar i becomes very small at iteration $k-1$, the gradient of its linearized buckling constraint approaches zero, shrinking the feasible region (Fig. 3a). As a result, these members cannot re-enter the design, and the SLP solver may stagnate in a local minimum. To overcome this, we introduce a heuristic *reinitialization* strategy that updates the areas used to compute the linearized constraints $\tilde{g}_{\text{buck}}$ at iteration k. This procedure is triggered whenever the solver reaches a local minimum, i.e., $||\Delta \boldsymbol{x}||_\infty \leq \text{tol}_{slp}$. Only members with area below a fraction τ of the maximum area $||\boldsymbol{a}^k||_\infty$ are modified. The updated values $\overline{\boldsymbol{a}}^k$ used to form the linearization point $\overline{\boldsymbol{P}}_k$ are :

$$\overline{a}_i^k := \begin{cases} \phi_n ||\boldsymbol{a}^k||_\infty, & a_i^k \leq \tau ||\boldsymbol{a}^k||_\infty, \\ a_i^k, & \text{otherwise.} \end{cases} \tag{8}$$

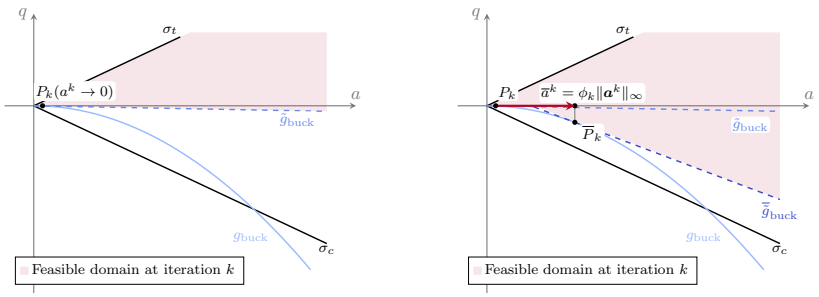

(a) (b)

FIGURE 3 – (a) Linearized buckling constraints restrict the feasible space for very small areas. (b) Reinitialization strategy expands the linearized domain by modifying the linearization point.

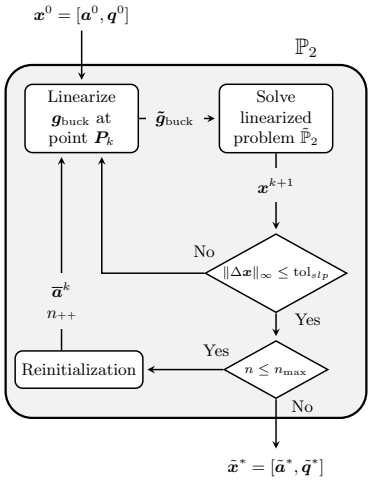

FIGURE 4 – SLP strategy with reinitialization used to solve Problem ($\mathbb{P}_2$).

As illustrated in Fig. 3b, updating $\tilde{g}_{\text{buck}}$ with $\bar{\bar{g}}_{\text{buck}}$ reduces the discrepancy between the original and linearized feasible regions, restoring nonzero gradients and enabling exploration of alternative designs.

The parameter ϕ_n in (8) controls the magnitude of reinitialization. To ensure convergence, we employ a continuation scheme :

$$\phi_n = \phi_{n-1}^{\beta}, \qquad n = 1, \ldots, n_{\max}, \tag{9}$$

where $n_{\max}$ is the maximum number of reinitialization calls and β governs the decay rate. Thus, the influence of reinitialization diminishes as the optimization progresses. The full SLP procedure with reinitialization is shown in Fig. 4, and yields the optimized SLP design vector $\tilde{x}^* = [\tilde{a}^*, \tilde{q}^*]$.

3.4 Second step : NLP optimization

If there is only one load case and the initial ground structure has no imposed symmetries, the SLP solution $\tilde{x}^*$ is statically determinate [15, 11]. In this case, displacements can be directly evaluated using equation (7), completing the optimization. Otherwise, the structure's stability must be checked by computing the Degree of Static Indeterminacy (DSI) using Maxwell's criterion :

$$DSI = N_{\text{el}} - N_{\text{DOF}} - r, \tag{10}$$

where r is the number of fixed DOFs. If $DSI \leq 0$, equation (5) suffices to compute the displacements. For $DSI > 0$, the truss is potentially statically indeterminate, and additional nonlinear compatibility constraints are required. The optimization is then repeated in a second stage, referred to as the NLP step (see Fig. 1).

To limit sensitivity to local minima, the NLP is performed on a reduced design space. The SLP solution $\tilde{x}^*$ is used to prune the ground structure by removing all members whose areas fall below the threshold

$$a_j < a_{\text{thr}}, \qquad a_{\text{thr}} = \chi \max(\tilde{a}^*), \tag{11}$$

with χ the cross-sectional area threshold parameter. A finite element analysis (FEA) based on the direct stiffness method provides an initial estimate of displacements and forces for the NLP. The initial displacement vector $\boldsymbol{U}_0$ is computed from

$$\boldsymbol{K}\boldsymbol{U}_0 = \boldsymbol{f}, \qquad \boldsymbol{K} = \boldsymbol{B}^\top \boldsymbol{D}\boldsymbol{B}, \qquad \boldsymbol{D} = \mathrm{diag}(E(\tilde{\boldsymbol{a}}^* + \delta \boldsymbol{e})/\boldsymbol{l}),$$

where $\boldsymbol{e} = [1, \ldots, 1]^\top$ and $\delta = 10^{-12}$. The small offset δ avoids singularity when the SLP solution forms mechanisms under load cases not considered in the SLP stage [5]. Initial member forces $\boldsymbol{q}_0$ are then evaluated via equation (5). The vectors $\tilde{\boldsymbol{a}}^*$, $\boldsymbol{q}_0$, and $\boldsymbol{U}_0$ serve as the initial point for the full NLP, where kinematic compatibility and exact local buckling constraints are reinstated. The NLP solver outputs the final optimized variables $\boldsymbol{x}^* = [\boldsymbol{a}^*, \boldsymbol{q}^*, \boldsymbol{U}^*]$.

4 Application to a 3D CRM wingbox

The bounding-volume nodes and applied loads follow the definitions in [16], where their evaluation is described in detail. The ground structure is shown in Fig. 5a. An aluminum alloy is used for the optimization, with material properties given in Table 1. Safety factors are applied to each load case by reducing the allowable stress and buckling limits by factors of 1.5, 1.5, and 2.67 for the three load cases (+2.5 g manouver, -1 g manouver, Cruise with gust +1.3 g). All members use circular cross-sections with buckling parameter $s = \pi E/4$. Optimization is carried out only on the internal wingbox structure ; skin effects are neglected. The relaxed LP Problem ($\tilde{\mathbb{P}}_2$) is solved using CVXPY 1.2.2 [17] with the ECOS 2.0.7 solver. The

E	σ_c, σ_t	ρ
69 GPa	$\pm$270 MPa	2.7 $\mathrm{g/m^3}$

TABLE 1 – Material data used for the CRM optimization.

full NLP Problem ($\mathbb{P}_1$) is solved using `cyipopt`, the Python interface to IPOPT 3.14.11, with PARDISO 6.0 as the linear solver. Convergence tolerances are

$$\|\Delta \mathbf{x}\|_\infty \leq \mathrm{tol}_{slp}, \qquad \|\Delta_{\mathrm{NLP}}\|_\infty \leq \mathrm{tol}_{nlp},$$

with $\mathrm{tol}_{slp} = 10^{-6}$ and $\mathrm{tol}_{nlp} = 10^{-4}$. Here, Δ_{NLP} denotes the scaled NLP error used by IPOPT to measure optimality and constraint residuals. The reinitialization parameter ϕ follows the continuation rule in (9). All scaling, SLP, and NLP parameters are listed in Table 2.

TABLE 2 – Values and description of the parameters used for the SLP and NLP optimizations

Parameter	Value	Description
$\mathrm{tol}_{\mathrm{SLP}}$	10^{-6}	Stopping criterion SLP
$\mathrm{tol}_{\mathrm{NLP}}$	10^{-4}	Stopping criterion NLP
$\mathrm{maxit}_{\mathrm{SLP}}$	400	Maximum iterations of the SLP algorithm
$\mathrm{maxit}_{\mathrm{NLP}}$	5000	Maximum iterations of the NLP algorithm
δ_{GS}	10^{-6}	Threshold for the ground structure reduction
δ_{reinit}	0.05	Threshold for the reinitialization
α_0	0.8	Initial reinitialization magnitude parameter
n	2	Index of the exponential decay law

4.1 Numerical optimization of the CRM wingbox

The optimized CRM-315 structure shows a mass of $21.342\,\mathrm{t}$, a 27.01% reduction compared to the solution with discrete cross-section areas found by [16] (29.238 tonne). Other than the substantial difference in the modelization of the cross-section areas, the mass reduction could be explained by the fact that the proposed algorithm allows members to vanish : our solution shows 257 active bars out of 315 at convergence (see Figure 5b). In contrast, the Mixed-Integer Linear Optimization (MILO) problem solved in [16] is employed as a sizing optimization algorithm with fixed topology (and thus 315 active members in the optimized design). Our solution offers also a drastic computational time reduction (147 s on a regular notebook vs over four days of optimization).

(a) (b)

FIGURE 5 – (a) Ground structure of the CRM-315 test case ; (b) Ground structure of the CRM-2370 test case. The cross-sectional areas shown in the two sub-figures represent the starting point of the optimizations. (c) Optimized topology of the CRM-315 with 257 active bars.

Material	**Aluminium**	**Titanium**	**Steel**	**Pultruted CFRP**
E	69 GPa	120 GPa	210 GPa	150 GPa
σ_c, σ_t	$\pm$270 MPa	$\pm$880 MPa	$\pm$355 MPa	+1200,-880 MPa
ρ	2.7 $[\mathrm{gr/cm^3}]$	4.5 $[\mathrm{gr/cm^3}]$	7.8 $[\mathrm{gr/cm^3}]$	1.6 $[\mathrm{gr/cm^3}]$
kg CO_2^{eq}/kg	12.5	47.0	5.0	34.5
\$/kg	2.2	23.5	6.3	40.5
$Mass$	21.34t	20.37t	46.16t	5.86t

TABLE 3 – Material data of the four materials used for the CRM-315 optimization.

4.2 Multiple materials

The proposed formulation uses material data as input for the optimization, and until this point, we have not investigated how material data could influence the topology and the final volume of the optimized structure. However, we recognize the importance of the choice of material properties, and here, we aim to examine their influence on the CRM-315 test case. The deformed structures in Figure 6, which

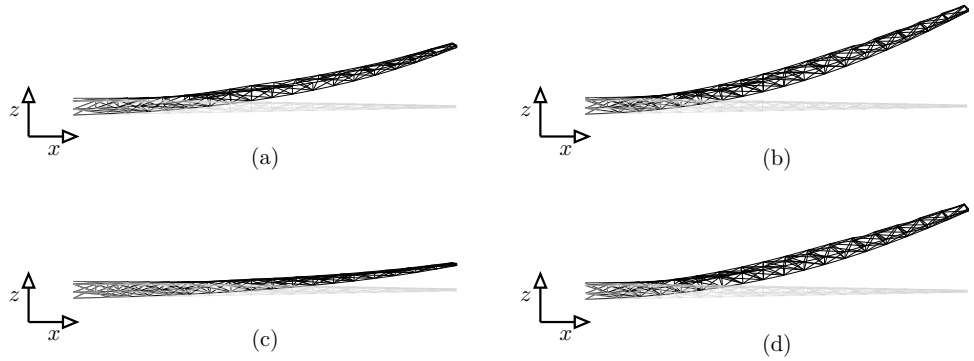

FIGURE 6 – Undeformed (gray) and deformed (black) shapes of the optimized CRM-315 structures with four different materials for the LC_1 load case ; (a) aluminum with $Z_t = 4.10\ [\mathrm{m}]$; (b) titanium with $Z_t = 5.97\ [\mathrm{m}]$; (c) stainless steel with $Z_t = 1.70\ [\mathrm{m}]$; (d) pultruded CFRP with $Z_t = 5.31\ [\mathrm{m}]$.

strongly highlights the highly deformed shapes obtained with titanium and pultruded CFRP, due to their superior resistance properties. The environmental and economic cost of the four structures is shown in Figure 7, we notice that, apart from titanium, the structures exhibit almost the same environmental cost for material production. This is unexpected given the significantly different specific CO2 emissions of the four materials ; there is nearly a seven-fold difference between steel and CFRP. However, the CFRP solution demonstrates a massive weight reduction, ultimately favoring it over steel and even aluminum.

Références

[1] N. B. Cramer, D. W. Cellucci, O. B. Formoso, et al. Elastic shape morphing of ultralight structures by programmable assembly. *Smart Materials and Structures*, 2019.

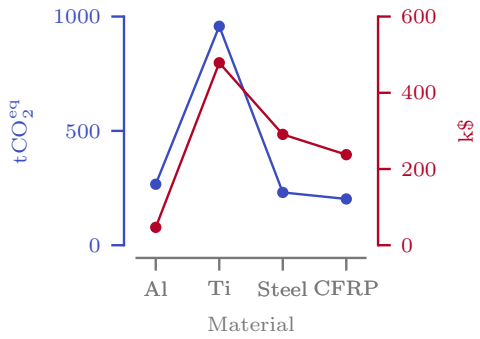

FIGURE 7 – Environmental and economic cost of the CRM-315 structure optimized using four different materials : aluminum, titanium, stainless steel, and pultruded CFRP.

[2] M. M. Opgenoord and K. E. Willcox. Aeroelastic tailoring using additively manufactured lattice structures. In *2018 Multidisciplinary Analysis and Optimization Conference*, Atlanta, Georgia, 2018. American Institute of Aeronautics and Astronautics.

[3] M. M. J. Opgenoord and K. E. Willcox. Design for additive manufacturing : cellular structures in early-stage aerospace design. *Structural and Multidisciplinary Optimization*, 60(2), 2019.

[4] M. Shahabsafa, A. Mohammad-Nezhad, T. Terlaky, et al. A novel approach to discrete truss design problems using mixed integer neighborhood search. *Structural and Multidisciplinary Optimization*, 58(6) :2411–2429, 2018.

[5] W. S. Dorn, R. E. Gomory, and H. Greenberg. Automatic design of optimal structures. *Journal de Mécanique*, 1964.

[6] G. Cheng. Some aspects of truss topology optimization. *Structural Optimization*, 10(3–4) :173–179, 1995.

[7] X. Guo, G. Cheng, and K. Yamazaki. A new approach for the solution of singular optima in truss topology optimization with stress and local buckling constraints. *Structural and Multidisciplinary Optimization*, 22(5) :364–373, 2001.

[8] M. Stolpe and K. Svanberg. A note on stress-constrained truss topology optimization. *Structural and Multidisciplinary Optimization*, 25(1) :62–64, 2003.

[9] M. P. Bendsøe. *Optimization of Structural Topology, Shape, and Material*. Springer Berlin Heidelberg, Berlin, 1995.

[10] W. Achtziger. Local stability of trusses in the context of topology optimization part ii : A numerical approach. *Structural Optimization*, 17(4) :247–258, 1999.

[11] G. I. N. Rozvany, M. P. Bendsøe, and U. Kirsch. Layout optimization of structures. *Applied Mechanics Reviews*, 48(2) :41–119, 1995.

[12] U. Kirsch. Optimal design of trusses by approximate compatibility. *Computers & Structures*, 12(1) :93–98, 1980.

[13] S. Sankaranarayanan, R. T. Haftka, and R. K. Kapania. Truss topology optimization with simultaneous analysis and design. *AIAA Journal*, 32(2) :420–424, 1994.

[14] J. Schwarz, T. Chen, K. Shea, and T. Stanković. Efficient size and shape optimization of truss structures subject to stress and local buckling constraints using sequential linear programming. *Structural and Multidisciplinary Optimization*, 58(1) :171–184, 2018.

[15] U. Kirsch. Optimal topologies of truss structures. *Computer Methods in Applied Mechanics and Engineering*, 72(1) :15–28, 1989.

[16] R. Fakhimi, M. Shahabsafa, W. Lei, S. He, J. R. R. A. Martins, T. Terlaky, and L. F. Zuluaga. Discrete multi-load truss sizing optimization : Model analysis and computational experiments. *Optimization and Engineering*, 2021.

[17] S. Diamond and S. Boyd. Cvxpy : A python-embedded modeling language for convex optimization, 2016. 5 pages.